

Probing spin and pseudospin symmetries in deformed nuclei by the Green's function method

Ting-Ting Sun^{1,2,*}, Bing-Xin Li,¹ and Kun Liu¹

¹*School of Physics and Microelectronics, Zhengzhou University, Zhengzhou 450001, China*

²*Guangxi Key Laboratory of Nuclear Physics and Nuclear Technology, Guangxi Normal University, Guilin 541004, China*



(Received 26 October 2023; accepted 3 January 2024; published 23 January 2024)

Spin and pseudospin symmetries play vital roles in nuclear physics and have been studied extensively in spherical nuclei. However, there are much fewer studies in deformed systems and there remain many open questions. In this work, for the first time, we examine the possible spin and pseudospin symmetries (SS and PSS) in deformed nuclei by solving a coupled-channels Dirac equation with the Green's function method, which provides a novel way to exactly determine the single-particle levels and properly describe the spacial density distributions. Taking axially deformed nucleus ^{154}Dy as an example, the spin doublets with a combination of Nilsson levels $\Lambda \pm 1/2[\mathcal{N}, n_z, \Lambda]$ and pseudospin doublets with a combination of $\tilde{\Lambda} \pm 1/2[\tilde{\mathcal{N}}, \tilde{n}_z, \tilde{\Lambda}]$ are determined. Different behaviors are displayed for the spin and pseudospin doublets. For the spin partners, those with smaller angular momentum l and the third component Λ owns better symmetry such as the $1p$ doublet while good pseudospin symmetry appears in partners locating close to the continuum threshold. By examining the single-particle Nilsson levels $\Omega[\mathcal{N}, n_z, \Lambda]$ and the energy splittings between the partners, the conservation and breaking of SS and PSS are examined at different deformations. In the prolate side, the Nilsson levels for the spin and pseudospin doublets are almost parallel and the energy splittings are stable against varying deformations. By examining the density distributions, great similarities have been observed in the upper components for the spin doublets while great similarities in the lower component for the pseudospin doublets. Besides, these similarities maintain well at different deformations.

DOI: [10.1103/PhysRevC.109.014323](https://doi.org/10.1103/PhysRevC.109.014323)

I. INTRODUCTION

Symmetries in the single-particle spectra of atomic nuclei are of great significance to nuclear structure and have been extensively discussed in the literature [1–4]. The breaking of spin symmetry (SS), i.e., the remarkable spin-orbit splitting for the spin doublets ($n, l, j = l \pm 1/2$) caused by the spin-orbit potential (SOP), laid the foundation for the understanding of the traditional magic numbers in nuclear physics [5,6]. Afterwards, based on the observation of the near-degeneracy in single-particle levels with quantum numbers ($n, l, j = l + 1/2$) and ($n - 1, l + 2, j = l + 3/2$), a new symmetry, namely the pseudospin symmetry (PSS) was introduced in nuclear physics, and the two levels are viewed as pseudospin doublets denoted by the pseudo quantum numbers ($\tilde{n} = n - 1, \tilde{l} = l + 1, j = \tilde{l} \pm 1/2$) [7,8]. Significantly, PSS has been used to explain a number of phenomena in nuclear structure such as nuclear deformation [9], superdeformation [10], magnetic moment [11], and identical rotational bands [12].

In the early years, comprehensive efforts were made to understand the origin of PSS. Apart from relabeling the quantum numbers, the explicit transformations from a normal state (l, s) to a pseudostate (\tilde{l}, \tilde{s}) were proposed in Refs. [13–15]. In 1997, Ginocchio made substantial progress and clearly

showed that PSS is a relativistic symmetry in the Dirac Hamiltonian and becomes exactly conserved when the attractive scalar and repulsive vector potentials are equal in size and opposite in sign, i.e., $\Sigma(r) \equiv S(r) + V(r) = 0$ [16]. He also claimed that the pseudo-orbital angular momentum \tilde{l} is nothing but the orbital angular momentum of the lower component of the Dirac wave function [16]. Meanwhile, the single-nucleon wave functions of the lower component for the pseudospin doublets exhibit some similarities [17]. However, the PSS is always broken in real nuclear systems due to the nonzero potentials $\Sigma(r)$. Later, Meng *et al.* proposed a more general condition $d\Sigma(r)/dr = 0$ for PSS, which can be approximately satisfied in exotic nuclei with highly diffused potentials [18]. Besides, he also pointed out that the extent of the conservation of PSS is connected with the competition between the pseudocentrifugal barrier (PCB) and the pseudospin-orbit potential (PSOP) [19]. Afterwards, the SS and PSS were studied extensively, e.g., PSS and SS in hypernuclei [20–24], SS in antinucleon spectra [25–28], PSS in the single-particle resonant states [29–37], perturbative interpretation of SS and PSS [38,39], and PSS in supersymmetric quantum mechanics [40,41].

PSS has also been observed in deformed nuclei [42]. In axially deformed nuclei, two single-particle orbitals with asymptotic Nilsson quantum numbers ($\Omega = \Lambda + 1/2[\mathcal{N}, n_3, \Lambda]$) and ($\Omega = \Lambda + 3/2[\mathcal{N}, \tilde{n}_3, \Lambda + 2]$) are redefined as a pseudospin doublet ($\tilde{\Omega} = \Lambda \pm 1/2[\tilde{\mathcal{N}} = \mathcal{N} - 1, \tilde{n}_3 = n_3, \tilde{\Lambda} = \Lambda + 1]$) due to the quasidegeneracy between

*ttsunphy@zzu.edu.cn

them [9]. To date, a series of works have been done to study the SS and PSS in deformed nuclei [43,44]. In Ref. [45], based on the relativistic mean-field (RMF) theory, Sugawara-Tanabe *et al.* pointed out for the first time that the PSS is always hidden in the unnatural parts of the Dirac wave function irrespective of the deformation. Later, they also found that both SS and PSS exist in the deformed nuclei and are respectively related to the upper and lower components of the Dirac wave functions [44]. In Ref. [46], the quasidegenerate pseudospin doublets were confirmed to exist near the Fermi surface for deformed nuclei by carrying out constrained deformed RMF calculations. In Ref. [47], the Dirac eigenfunctions in the RMF calculations of deformed nuclei were examined extensively. In Ref. [48], based on the similarity renormalization group theory, Guo *et al.* investigated the pseudospin symmetry in deformed nuclei and confirmed the crucial role of the nonrelativistic term, the spin-orbit term, and the dynamical term. In Ref. [49], based on the complex momentum representation (CMR) method, the PSS in resonant states was explored in deformed nuclei and found to be approximately reserved with small splittings for energies, widths, and density distributions.

In recent years, Green's function (GF) method has achieved great successes in describing continuum and has been widely applied in nuclear physics, such as in the studies of single-particle structures including the resonant states [35,50–54], halos in exotic nuclei [55–58], and collective excitations [59–64]. This method is very convenient to use in combination with different nuclear models. In 2014, we applied the Green's function method to the RMF theory (RMF-GF) to investigate the single-particle resonant states for the first time [50]. In 2016, by further including the pairing correlation, we applied the Green's function method to the relativistic continuum Hartree-Bogoliubov theory (RCHB-GF) to study halo phenomena [57]. In 2019, by including the blocking effects, we extended the self-consistent Green's function continuum Skyrme-Hartree-Fock-Bogoliubov theory [56] to the descriptions of odd-*A* nuclei [58,65]. In 2020, by further including the deformation, we applied the Green's function method to solve a coupled-channels Dirac equation with axially quadrupole deformed potentials, and we analyzed the deformed halo in ^{37}Mg [66]. According those studies, the Green's function method has shown great advantages, such as treating the single-particle bound states and the continuum on the same footing, determining directly the energies and widths for resonances, and describing properly the the spatial density distributions. Recently, based on the Green's function method, a novel way by searching for the extremes of the density of states [67] or the poles of Green's function [68] has been proposed to determine the resonant states, which can exactly determine the energies and widths for the bound and resonant states regardless of the width. Besides, this method can describe the resonant states in any potential without any requirement on the potential shape. As an application, the conservation and breaking of PSS in the single-nucleon resonant states have been examined from the PSS limit to finite depth potentials, and in the PSS limit, besides strictly the same energies and widths between the PS partners, identical density distributions of the lower component were found for the first

time [69]. Furthermore, a uniform description of pseudospin symmetry in bound and resonant states has been given [70].

In this work, the possible SS and PSS of single-particle bound states in deformed nuclei are examined by the Green's function method. The effects of deformation on these symmetries are discussed. The paper is organized as follows. The theoretical framework of the Green's function method for solving the coupled-channel Dirac equation is presented in Sec. II. After the numerical details in Sec. III, Sec. IV is devoted to the discussions of the numerical results, where the conservation and breaking of the SS and PSS in deformed nuclei are illustrated by analyzing the energy splittings and the density distributions. Finally, a summary is given in Sec. V.

II. THEORETICAL FRAMEWORK

To explore the SS and PSS in deformed nuclei with the RMF theory, the Dirac equations governing the motion of the nucleons will be examined:

$$\{\boldsymbol{\alpha} \cdot \mathbf{p} + V(\mathbf{r}) + \beta[M + S(\mathbf{r})]\}\psi(\mathbf{r}) = \varepsilon\psi(\mathbf{r}), \quad (1)$$

where $\boldsymbol{\alpha}$ and β are Dirac matrices, M is the mass of nucleon, and $S(\mathbf{r})$ and $V(\mathbf{r})$ are the scalar and vector potentials, respectively, which are adopted as the axially quadrupole-deformed potentials,

$$S(\mathbf{r}) = S_0(r) + S_2(r)Y_{20}(\theta, \phi), \quad (2a)$$

$$V(\mathbf{r}) = V_0(r) + V_2(r)Y_{20}(\theta, \phi), \quad (2b)$$

with $S_0(r)$ and $V_0(r)$ being the spherical components while $S_2(r)Y_{20}(\theta, \phi)$ and $V_2(r)Y_{20}(\theta, \phi)$ are the quadrupole parts.

For a nucleon in an axially quadrupole-deformed potential, parity π and the z component Ω of the angular momentum are good quantum numbers, and the single-particle wave function can be expanded in terms of spherical Dirac spinors,

$$\psi_\Omega = \sum_\kappa \begin{pmatrix} i \frac{G_{\Omega\kappa}(r)}{r} \\ \frac{F_{\Omega\kappa}(r)}{r} \sigma \cdot \hat{\mathbf{r}} \end{pmatrix} Y_{\kappa\Omega}(\theta, \phi), \quad (3)$$

where $G_{\Omega\kappa}(r)/r$ and $F_{\Omega\kappa}(r)/r$ are, respectively, the radial wave functions for the upper and lower components, $Y_{\kappa\Omega}(\theta, \phi)$ are the spinor spherical harmonics, and the quantum number κ is related with the orbital angular momenta l and the total angular momenta j ,

$$\begin{aligned} l = \kappa, j = \kappa - \frac{1}{2} & \quad \text{if } \kappa > 0, \\ l = -\kappa - 1, j = -\kappa - \frac{1}{2} & \quad \text{if } \kappa < 0, \end{aligned} \quad (4)$$

which labels different spherical partial waves or ‘‘channels.’’

Then the Dirac equation (1) is transformed into a coupled-channels form of radial wave functions,

$$\begin{aligned} 0 = \frac{dG_{\Omega\kappa}}{dr} + \frac{\kappa}{r}G_{\Omega\kappa} - (\varepsilon_\Omega + 2M)F_{\Omega\kappa} \\ + \sum_{\kappa'\lambda} (V_\lambda - S_\lambda)A(\lambda, \kappa', \kappa, \Omega)F_{\Omega\kappa'}, \end{aligned} \quad (5a)$$

$$\begin{aligned} 0 = \frac{dF_{\Omega\kappa}}{dr} - \frac{\kappa}{r}F_{\Omega\kappa} + \varepsilon_\Omega G_{\Omega\kappa} \\ - \sum_{\kappa'\lambda} (V_\lambda + S_\lambda)A(\lambda, \kappa', \kappa, \Omega)G_{\Omega\kappa'}, \end{aligned} \quad (5b)$$

where the couplings among different spherical channels are governed by the deformed potentials,

$$v_{\kappa\kappa'}^{\pm} = \sum_{\lambda} (V_{\lambda} \pm S_{\lambda}) A(\lambda, \kappa', \kappa, \Omega), \quad (6)$$

in which the index $\lambda = 0$ and 2 , respectively, for the spherical and quadrupole parts of the potentials, and $A(\lambda, \kappa', \kappa, \Omega)$ can be expressed as

$$\begin{aligned} A(\lambda, \kappa', \kappa, \Omega) &= \langle Y_{\kappa\Omega} | Y_{\lambda 0} | Y_{\kappa'\Omega} \rangle \\ &= (-1)^{\Omega+\frac{1}{2}} \frac{\hat{j}\hat{j}'}{\sqrt{4\pi}} \begin{pmatrix} j & \lambda & j' \\ -\Omega & 0 & \Omega \end{pmatrix} \begin{pmatrix} j' & \lambda & j \\ \frac{1}{2} & 0 & -\frac{1}{2} \end{pmatrix}, \end{aligned} \quad (7)$$

with $\hat{j} = \sqrt{2j+1}$. In the practical calculations, we must truncate the partial-wave expansion and use N to represent the number of spherical partial waves to be included for a given block Ω^{π} . Besides, note that the single-particle energy in Eq. (5) is shifted by M with respect to that in Eq. (1).

Applying the Green's function method to solve the coupled-channels Dirac Eq. (5), a Green's function will be constructed, defined as

$$[\varepsilon - \hat{h}(\mathbf{r})] \mathcal{G}(\mathbf{r}, \mathbf{r}'; \varepsilon) = \delta(\mathbf{r} - \mathbf{r}'), \quad (8)$$

where $\hat{h}(\mathbf{r})$ is the Dirac Hamiltonian and ε is an arbitrary single-particle energy. In the axially quadrupole-deformed potential, using the partial-wave expansion, the Green's function with a given Ω can be expanded as

$$\mathcal{G}_{\Omega}(\mathbf{r}, \mathbf{r}'; \varepsilon) = \sum_{\kappa\kappa'} Y_{\kappa\Omega}(\theta, \phi) \frac{\mathcal{G}_{\Omega\kappa\kappa'}(r, r'; \varepsilon)}{r r'} Y_{\kappa'\Omega}^*(\theta', \phi'), \quad (9)$$

where $\mathcal{G}_{\Omega\kappa\kappa'}(r, r'; \varepsilon)$ is the radial Green's function coupling the partial waves κ and κ' , and it is in a $2N \times 2N$ matrix form,

$$\mathcal{G}_{\Omega\kappa\kappa'}(r, r'; \varepsilon) = \begin{pmatrix} \mathcal{G}_{\Omega\kappa\kappa'}^{(11)}(r, r'; \varepsilon) & \mathcal{G}_{\Omega\kappa\kappa'}^{(12)}(r, r'; \varepsilon) \\ \mathcal{G}_{\Omega\kappa\kappa'}^{(21)}(r, r'; \varepsilon) & \mathcal{G}_{\Omega\kappa\kappa'}^{(22)}(r, r'; \varepsilon) \end{pmatrix}. \quad (10)$$

According to the definition in Eq. (8), the radial Green's function $\mathcal{G}_{\Omega\kappa\kappa'}(r, r'; \varepsilon)$ satisfies the following coupled-channels equation:

$$\begin{aligned} \begin{pmatrix} -\varepsilon & -\frac{d}{dr} + \frac{\kappa}{r} \\ \frac{d}{dr} + \frac{\kappa}{r} & -\varepsilon - 2M \end{pmatrix} \mathcal{G}_{\Omega\kappa\kappa'}(r, r'; \varepsilon) \\ + \sum_{\kappa''} \begin{pmatrix} v_{\kappa\kappa''}^{+} & 0 \\ 0 & v_{\kappa\kappa''}^{-} \end{pmatrix} \mathcal{G}_{\Omega\kappa''\kappa'}(r, r'; \varepsilon) = \frac{\delta(r - r')}{r r'} J, \end{aligned} \quad (11)$$

where

$$J = \begin{pmatrix} 1 & 0 \\ 0 & -1 \end{pmatrix} \otimes I_N, \quad (12)$$

with I_N being the N -dimensional unit matrix.

For the single-particle bound states, the density of states (DoS) $n(\varepsilon)$ exhibits discrete δ functions and can be easily expressed as

$$n(\varepsilon) = \sum_n \delta(\varepsilon - \varepsilon_n), \quad (13)$$

where ε is a real single-particle energy and ε_n represents the eigenvalues of the Dirac equation. With an infinitesimal imaginary part "i ϵ " to the real energy ε , $n(\varepsilon)$ can be calculated by integrating the imaginary part of the Green's function in the coordinate space. For a given block Ω^{π} , it can be expressed as

$$\begin{aligned} n_{\Omega}(\varepsilon) &= -\frac{2}{\pi} \sum_k \int dr \text{Im} [\mathcal{G}_{\Omega\kappa\kappa}^{(11)}(r, r; \varepsilon + i\epsilon) + \mathcal{G}_{\Omega\kappa\kappa}^{(22)}(r, r; \varepsilon + i\epsilon)]. \end{aligned} \quad (14)$$

With the infinitesimal imaginary part "i ϵ ", the DoSs for discrete single-particle states in forms of δ functions (no width) are simulated by Lorentzian functions with the full width at half maximum (FWHM) of 2ϵ .

For the constructions of the Green's function and other details in solving the couple-channel Dirac equations with the Green's function method, refer to our previous work in Ref. [66].

III. NUMERICAL DETAILS

In the present study, potentials in Woods-Saxon forms for the radial part of the quadrupole deformed potentials in Eq. (2) are adopted as [71,72]

$$\begin{aligned} S_0(r) &= S_{\text{WS}} f(r), \quad V_0(r) = V_{\text{WS}} f(r), \\ S_2(r) &= -\beta S_{\text{WS}} k(r), \quad V_2(r) = -\beta V_{\text{WS}} k(r), \end{aligned} \quad (15)$$

with

$$f(r) = \frac{1}{1 + \exp(\frac{r-R}{a})} \quad \text{and} \quad k(r) = r \frac{df(r)}{dr}. \quad (16)$$

To study the behavior of SS and PSS in the single-particle spectra, as an example we take the nucleus ^{154}Dy , which has a stable axially deformation of $\beta = 0.24$ [73]. The mean-field Woods-Saxon potentials are adopted with the depths of the scalar and vector potentials $S_{\text{WS}} = -405.0$ MeV and $V_{\text{WS}} = 350.0$ MeV, the radius $R = 6.81$ fm, and the diffuseness $a = 0.67$ fm following Ref. [48].

To solve the coupled-channels Dirac equation in the coordinate space, a space size of $R_{\text{box}} = 20$ fm and a mesh step of 0.1 fm are taken. For calculating the density of states $n_{\Omega}(\varepsilon)$, the infinitesimal parameter ϵ in Eq. (14) is taken as 1.0×10^{-6} MeV and the energy step $d\varepsilon$ is 1.0×10^{-3} MeV. With those parameters, the accuracy of the obtained single-particle energies can be up to 1.0 keV. Furthermore, a higher degree of accuracy can be achieved for energies if a smaller energy steps $d\varepsilon$ is taken.

IV. RESULTS AND DISCUSSION

With the Green's function method, the single-particle spectrum can be exactly determined both for the bound and resonant states by searching for the poles of Green's functions or extremes of density of states. In Fig. 1, the density of states $n_{\Omega}(\varepsilon)$ for deformed nucleus ^{154}Dy with $\Omega^{\pi} = 1/2^{\pm}, 3/2^{\pm}, 5/2^{\pm}$, and $7/2^{\pm}$ are plotted as functions of single-particle

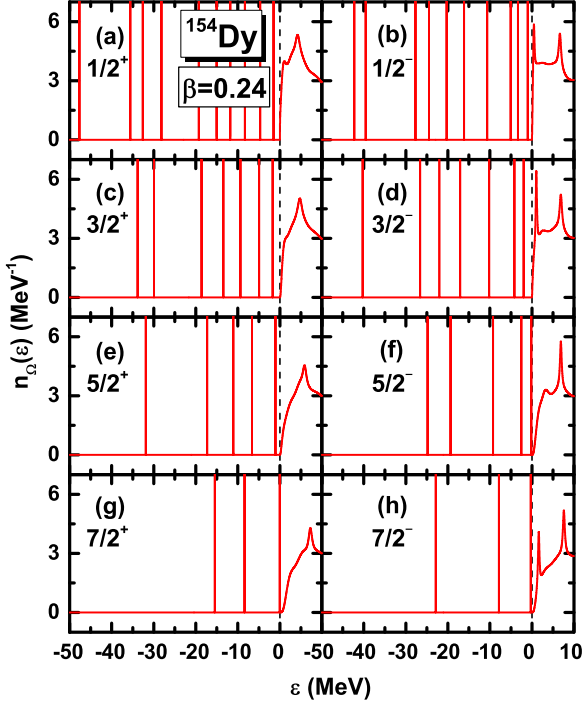


FIG. 1. Density of states $n_0(\epsilon)$ for nucleus ^{154}Dy with blocks $\Omega^\pi = 1/2^\pm, 3/2^\pm, 5/2^\pm,$ and $7/2^\pm$, obtained by solving the coupled-channels Dirac equations with quadrupole-deformed Woods-Saxon potentials using the GF method. The deformation parameter $\beta = 0.24$ and the number of coupled partial waves $N = 8$ are chosen. The dashed lines denote the continuum threshold.

energies ϵ obtained by solving the coupled-channels Dirac equation with the Green's function method, where the deformation parameter $\beta = 0.24$ and the number of coupled partial waves $N = 8$. The peaks in δ -function shape below the continuum threshold ($\epsilon = 0$) correspond to the single-particle bound states, and the spectra with $\epsilon > 0$ describe the continuum with peaks therein being the single-particle resonant states. For the single-particle bound states, the energies could be well determined directly by reading the locations of the extremes of the DoSs. For the single-particle resonant states, DoSs will be calculated on the complex energy plane $\epsilon = \epsilon_r + i\epsilon_i$ by scanning energies along both the real ϵ_r and imaginary ϵ_i axes. For the details, refer to Refs. [66,67].

In Table I, taking the blocks $\Omega^\pi = 1/2^+$ and $1/2^-$ as examples, the single-particle energies ϵ of the bound states extracted from Fig. 1 are listed, labeled by Nilsson quantum numbers $\Omega[\mathcal{N}, n_z, \Lambda]$ with \mathcal{N} being the principal quantum number, n_z the number of nodes of the wave functions in the z direction, and Λ the projection of the orbital angular momentum l onto the z axis. The nine positive parity states from top to bottom are split from the spherical $1s_{1/2}, 1d_{5/2}, 1d_{3/2}, 2s_{1/2}, 1g_{9/2}, 1g_{7/2}, 2d_{5/2}, 2d_{3/2},$ and $3s_{1/2}$ states, respectively. Similarly, the ten negative parity states are split from the $1p_{3/2}, 1p_{1/2}, 1f_{7/2}, 1f_{5/2}, 2p_{3/2}, 2p_{1/2}, 1h_{11/2}, 1h_{9/2}, 2f_{7/2},$ and $3p_{3/2}$ states, respectively. As shown in Table I, energies for the bound states in a deformed Dirac equation could be

TABLE I. Single-particle energies ϵ (in MeV) for the bound states in ^{154}Dy with $\Omega^\pi = 1/2^+$ and $1/2^-$ extracted from the density of states shown in Fig. 1.

$\Omega[\mathcal{N}n_z\Lambda]$	"+"parity	$\Omega[\mathcal{N}n_z\Lambda]$	"minus"parity
1/2[000]	-47.681	1/2[110]	-42.268
1/2[220]	-35.556	1/2[101]	-39.538
1/2[211]	-32.605	1/2[330]	-27.708
1/2[200]	-28.175	1/2[321]	-24.475
1/2[440]	-19.295	1/2[310]	-20.314
1/2[431]	-15.031	1/2[301]	-16.150
1/2[420]	-11.810	1/2[550]	-10.661
1/2[411]	-8.314	1/2[541]	-5.057
1/2[400]	-4.665	1/2[530]	-3.311
		1/2[510]	-1.008

effectively obtained by the Green's function method. This method can also strictly determine the energies and widths for resonant states. However, in this work, we will not talk much about the resonant states but mainly focus on the bound states.

In the following, the SS and PSS in deformed nuclei are examined for the single-particle bound states. In Fig. 2, taking ^{154}Dy as an example, we give the spin doublets as a

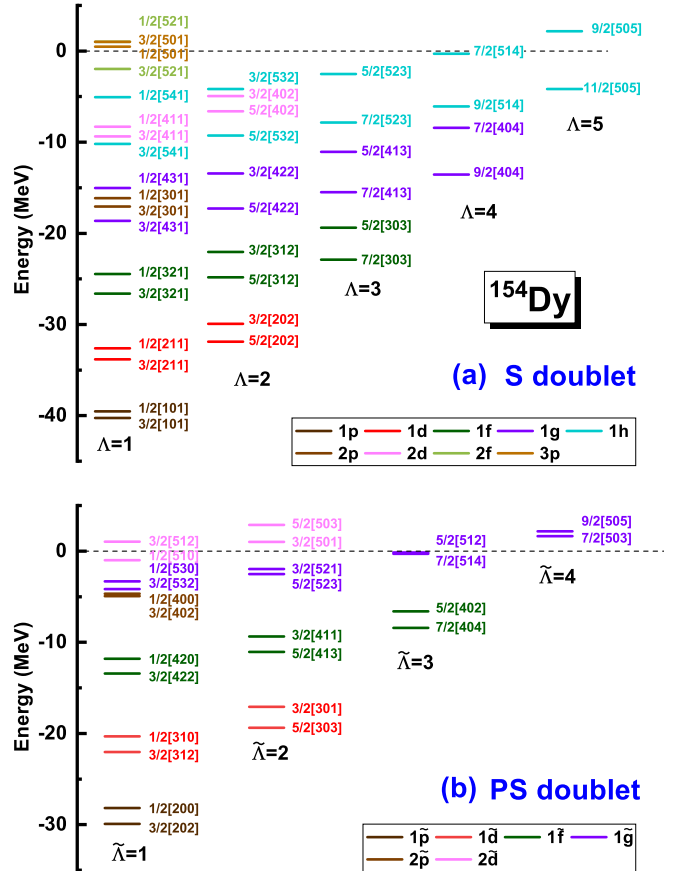


FIG. 2. Spin doublets $\Lambda \pm 1/2[\mathcal{N}n_z\Lambda]$ and pseudospin doublets $\tilde{\Lambda} \pm 1/2[\tilde{\mathcal{N}}, n_z, \Lambda]$ in ^{154}Dy .

combination of Nilsson levels with quantum numbers $\Omega = \Lambda + 1/2[\mathcal{N}, n_z, \Lambda]$ and $\Omega = \Lambda - 1/2[\mathcal{N}, n_z, \Lambda]$ and pseudospin doublets as a combination of Nilsson levels with quantum numbers $\Omega = \Lambda + 1/2[\mathcal{N}, n_z, \Lambda]$ and $\Omega = \Lambda + 3/2[\mathcal{N}, n_z, \Lambda + 2]$. The partners with the same Λ or $\tilde{\Lambda} = \Lambda + 1$ are put in the same column and those with the same (pseudo) principal quantum number n (\tilde{n}) and (pseudo) orbital angular momentum l (\tilde{l}) are denoted in the same color. For spin doublets, the following points could be revealed: (i) For partners with the same Λ , the SS becomes worse with increasing orbital angular momentum l , showing greater energy differences between the partners. In the case of $\Lambda = 1$, the energy differences are respectively 0.73, 1.23, 2.14, 3.59, and 5.14 MeV for the $1p$, $1d$, $1f$, $1g$, and $1h$ spin doublets. (ii) For partners with the same n and l , SS deteriorates with larger Λ , e.g., the energy differences of the $1g$ doublets corresponding to $\Lambda = 1, 2, 3, 4$ are respectively 3.59, 3.85, 4.43, and 5.14 MeV for the $(1/2[431], 3/2[431])$, $(3/2[422], 5/2[422])$, $(5/2[413], 7/2[413])$, and $(7/2[404], 9/2[404])$ spin doublets. (iii) When entering the continuum, an inversion of energy levels occurs for the spin doublet with the spin down state being lower than the spin up state, such as the partner $(1/2[501], 3/2[501])$.

However, different behaviors are displayed for the pseudospin doublets: (i) For partners with the same $\tilde{\Lambda}$, the PSS is better maintained with increasing pseudo-orbital angular momentum \tilde{l} . In the case of $\tilde{\Lambda} = 1$, the energy differences between the PS partners are respectively 1.75, 1.73, 1.62, and 0.86 MeV for the $1\tilde{p}$, $1\tilde{d}$, $1\tilde{f}$, and $1\tilde{g}$ PS doublets. (ii) For partners with the same \tilde{n} and \tilde{l} , the evolutions of the PSS with $\tilde{\Lambda}$ show different behaviors: for the $1\tilde{p}$ and $1\tilde{d}$ PS partners, PSS becomes worse with increasing $\tilde{\Lambda}$ while it improves significantly for the $1\tilde{f}$ PS partners. (iii) There is an obvious threshold effect, i.e., when the PS partner approaches the continuum threshold, PSS becomes much better and is conserved approximately. (iv) As in the spin doublet, when entering the continuum, an inversion of energy levels occurs for the PS doublet with the pseudospin down state being lower compared with the pseudospin up state, such as the partners $(1/2[510], 3/2[512])$, $(3/2[501], 5/2[503])$, and $(7/2[503], 9/2[505])$.

To explore the effects of deformation for the SS and PSS, in Fig. 3, the single-particle Nilsson levels $\Omega[\mathcal{N}n_z\Lambda]$ as a function of deformation parameter β are plotted ranging from $\beta = -0.4$ to 0.6. The solid and dashed lines are respectively for the levels with positive and negative parities. In the spherical case with $\beta = 0$, a distinct shell structure emerges with the traditional magic numbers 2, 8, 20, 28, 50, and 82, and seven pairs of spin doublets, i.e., $1p$, $1d$, $1f$, $2p$, $1g$, $2d$, and $1h$, are obtained. With the quadrupole deformations, as a result of levels splitting, more pairs of spin doublets are obtained as a combination of Nilsson levels with quantum numbers $\Omega = \Lambda - 1/2[\mathcal{N}, n_z, \Lambda]$ and $\Omega = \Lambda + 1/2[\mathcal{N}, n_z, \Lambda]$. On closer inspection, in the side of prolate deformations with β ranging from 0 to 0.6, the single-particle levels of spin doublets are approximately parallel, such as the spin doublets $1d$ ($3/2[202], 5/2[202]$), $1f$ ($5/2[303], 7/2[303]$), and $2p$ ($1/2[301], 3/2[301]$). However, this relationship does not exist well in the side of $\beta < 0$ with oblate deformation.

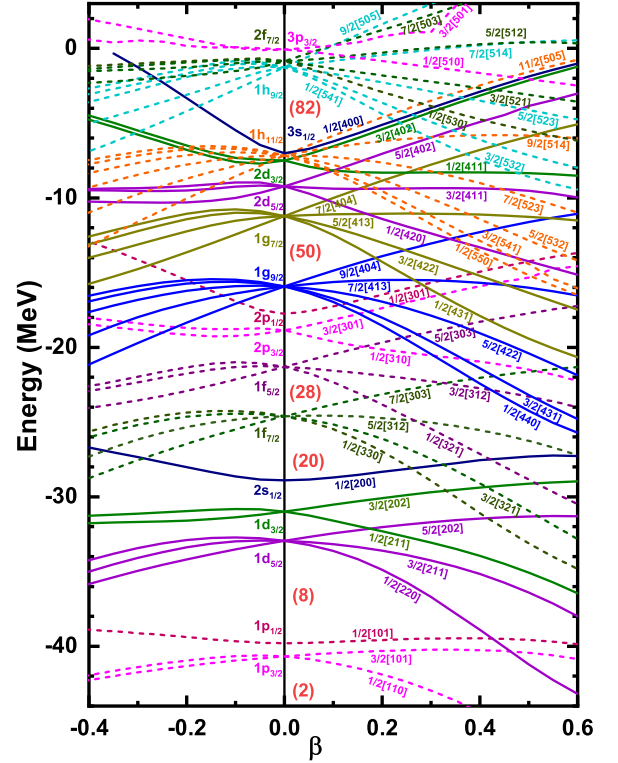


FIG. 3. Nilsson single-particle levels $\Omega[\mathcal{N}, n_z, \Lambda]$ as a function of deformation parameter β in quadrupole-deformed Woods-Saxon potentials. The solid and dashed lines denote levels with positive and negative parities, respectively.

In order to better master the SS in the deformed nuclei, in Fig. 4, the energy splittings $\Delta\varepsilon = \varepsilon_{\Omega_-} - \varepsilon_{\Omega_+}$ for the spin doublets $\Lambda \pm 1/2[\mathcal{N}, n_z, \Lambda]$ are plotted as a function of deformation β , where ε_{Ω_-} and ε_{Ω_+} are the energies of the spin

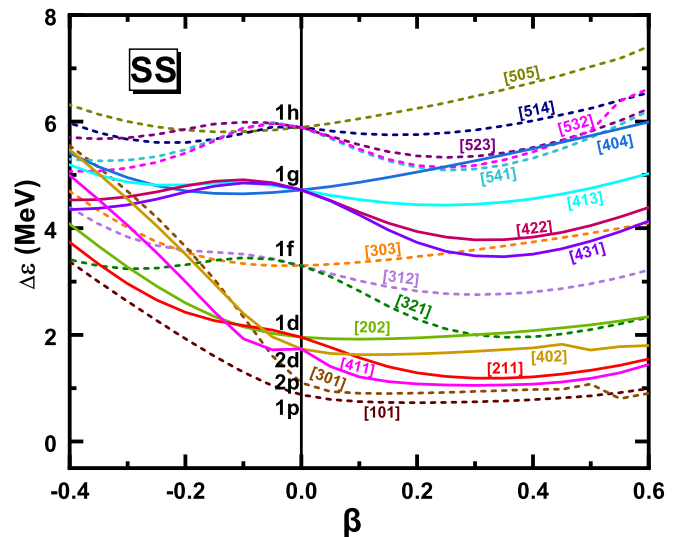


FIG. 4. Energy splittings $\Delta\varepsilon$ between the spin doublets $\Lambda \pm 1/2[\mathcal{N}, n_z, \Lambda]$ as a function of the deformation parameter β . The solid and dashed lines indicate doublets with positive and negative parities, respectively.

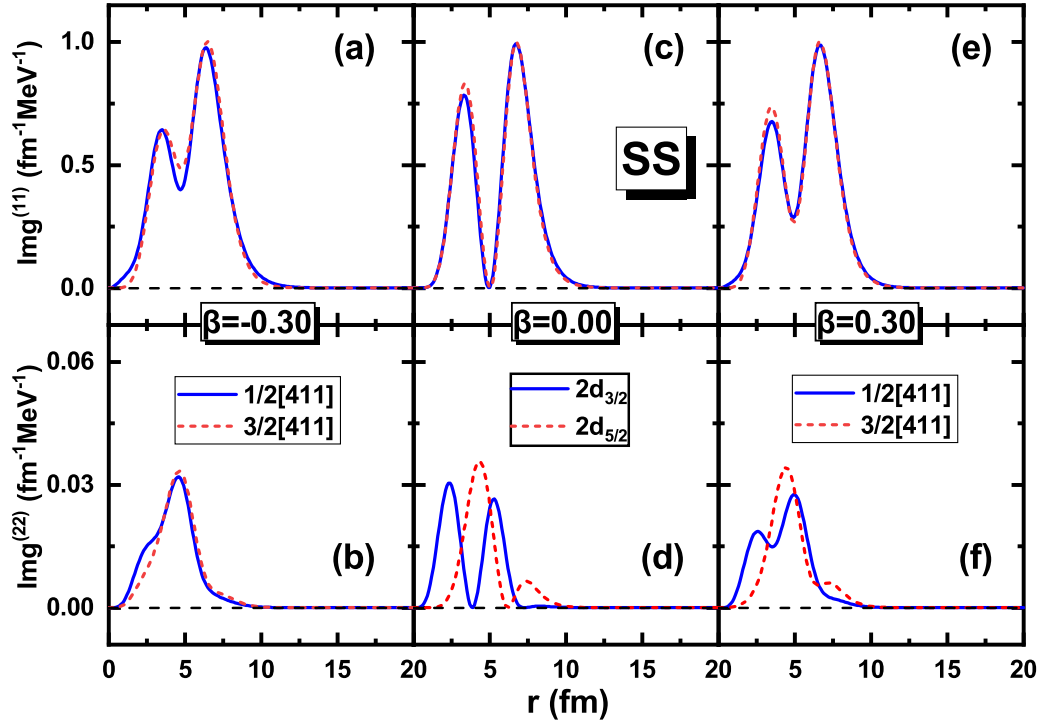


FIG. 7. Density distributions in the coordinate space, $\text{Im}G_k^{(11)}$ and $\text{Im}G_k^{(22)}$, for the $2d$ ($1/2[411]$, $3/2[411]$) spin doublets with different deformation parameters $\beta = -0.30$ (a,b), 0.00 (c,d), and 0.30 (e,f).

splitting between PS partners stays almost constant for most of the pseudospin doublets.

For a pair of (pseudo)spin doublet, the good (P)SS results in not only a (quasi)degeneracy in their energies, but also great

similarities in their Dirac wave functions. For the spin doublets, the upper components of the Dirac spinor $G(r)$ behave similarly, and for the pseudospin doublets, the lower components of the Dirac spinor $F(r)$ are similar. In the PSS limit,

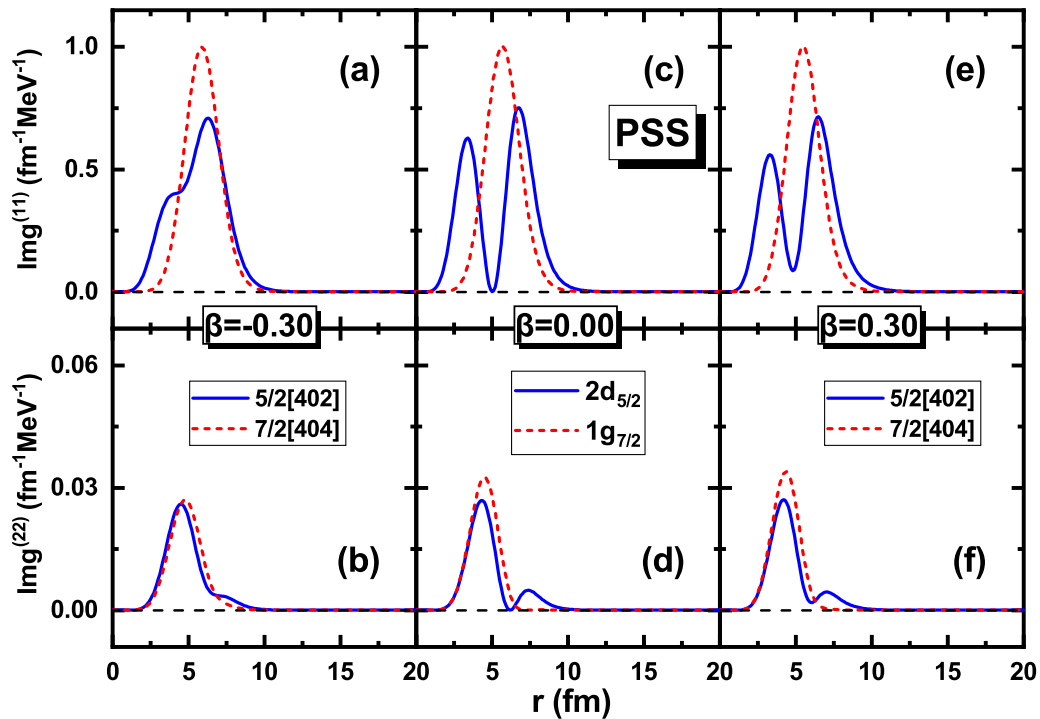


FIG. 8. The same as Fig. 7, but for the pseudospin doublet $1\tilde{f}$ ($5/2[402]$, $7/2[404]$).

i.e., when the attractive scalar and repulsive vector potentials have the same magnitude but opposite sign, identical density distributions of the lower components have been proved for the PS partners [69]. With the Green's function method, the density distributions in the coordinate space can be used to study the similarities of Dirac spinors and in the deformed nuclei, the radial density distributions corresponding to the upper and lower components of the Dirac wave functions for the single-particle state with Ω^π at the eigenvalues of ε could be calculated by

$$\rho_\Omega^{(g)}(r, \varepsilon) = -\frac{1}{4\pi r^2} \sum_\kappa \text{Im} \mathcal{G}_{\Omega\kappa\kappa}^{(11)}(r, r; \varepsilon), \quad (17)$$

$$\rho_\Omega^{(f)}(r, \varepsilon) = -\frac{1}{4\pi r^2} \sum_\kappa \text{Im} \mathcal{G}_{\Omega\kappa\kappa}^{(22)}(r, r; \varepsilon), \quad (18)$$

where different spherical partial waves are coupled together.

In Fig. 7, taking the spin doublets $2d(1/2[411], 3/2[411])$ as examples, the density distributions $\rho_\Omega^{(g)}(r, \varepsilon)$ and $\rho_\Omega^{(f)}(r, \varepsilon)$ are plotted at different deformations $\beta = -0.3, 0.0, 0.3$. In the spherical case, great similarities are observed in $\text{Im} \mathcal{G}_\kappa^{(11)}$ corresponding to the upper component of Dirac wave functions while a big difference exists in the lower component $\text{Im} \mathcal{G}_\kappa^{(22)}$ between the spin partners. All those together with a small energy splitting support the approximate spin symmetry. When the mean field potential deviates from the spherical shape, good consistency in $\text{Im} \mathcal{G}_\kappa^{(11)}$ between the spin doublets still stays at a prolate deformation of $\beta = 0.30$ while some more differences happen at the oblate deformation of $\beta = -0.3$. As seen in Fig. 4, the energy splitting between the spin doublets $2d(1/2[411], 3/2[411])$ is small in the side of prolate deformation and it remains stable with the increase of β from 0 to 0.6, while in the oblate side great differences are revealed at various deformations for the SS doublets, especially for those with low angular momentum.

In Fig. 8, we show the density distributions of the PSS doublets $1f(5/2[402], 7/2[404])$ at different deformations $\beta = -0.3, 0.0, 0.3$. In the spherical case, some similarities are revealed in the density distributions $\text{Im} \mathcal{G}_\kappa^{(22)}(r, \varepsilon)$ of the PSS doublets while one node difference, i.e., $n(2d_{5/2}) = n(1g_{7/2}) + 1$, is observed in the density distributions $\text{Im} \mathcal{G}_\kappa^{(11)}(r, \varepsilon)$ corresponding to the upper component of the Dirac wave functions. In the deformed case, the similarities in the lower component of the Dirac wave function remain, while the node relationship in the upper component $\text{Im} \mathcal{G}_\kappa^{(11)}(r, \varepsilon)$ is no longer satisfied.

V. SUMMARY

In this work, Green's function method has been applied to examine the possible spin and pseudospin symmetries in deformed nuclei for the first time, which provides a novel way to exactly determine the single-particle energies and also properly describe the density distributions.

First, taking the axially deformed nucleus ^{154}Dy as an example, the densities of states are calculated with the Green's

functions method by solving the coupled-channels Dirac equation with quadrupole-deformed Woods-Saxon potentials. By searching for the extremes of DoSSs, the single-particle energies for ^{154}Dy are exactly obtained, based on which the spin doublets $\Lambda \pm 1/2[\mathcal{N}, n_z, \Lambda]$ and pseudospin doublets $\tilde{\Lambda} \pm 1/2[\tilde{\mathcal{N}}, \tilde{n}_z, \tilde{\Lambda}]$ are determined. Different behaviors are displayed for the spin and pseudospin doublets. SS for doublets with the same Λ deteriorates with increasing l and, for those with the same n and l , it also becomes worse for larger Λ . Differently, PSS for doublets with the same $\tilde{\Lambda}$ is better maintained with increasing \tilde{l} and, for those with the same \tilde{n} and \tilde{l} , it sometimes becomes better for larger $\tilde{\Lambda}$. Besides, a great threshold effect is exhibited for PSS. One common point for the spin and pseudospin doublets is the inversions of energy levels between the partners observed in the area of continuum.

Second, to explore the effects of deformation for the SS and PSS, the single-particle Nilsson levels $\Omega[\mathcal{N}, n_z, \Lambda]$ are plotted as a function of deformation ranging from $\beta = -0.4$ to 0.6. By studying the energy splittings between the partners, the conservation and breaking of SS and PSS are examined at different deformations. In the side of prolate deformations with $\beta > 0$, the Nilsson levels for the spin and pseudospin doublets are almost parallel and the energy splittings are stable against different deformations. However, the energy splitting is very sensitive to the deformation β in the oblate side with $\beta < 0$. For the spin doublets, the energy splitting for the bound states stays positive over the whole range of deformation. The same conclusion is obtained for pseudospin doublets except those close to the continuum threshold. Besides, good spin symmetry may appear for partners with smaller angular momentum such as $1p$ partners, while good pseudospin symmetry appears in the states which locate close to the continuum threshold.

Finally, the density distributions in the coordinate space are plotted for the spin and pseudospin doublets at different deformations $\beta = -0.3, 0, 0.3$. For the spin doublets, great similarities are observed for the $\rho_\Omega^{(g)}(r, \varepsilon)$, which is related to the upper component of the Dirac wave functions, while great similarities are observed for the density distribution $\rho_\Omega^{(f)}(r, \varepsilon)$, which is related to the lower component of the Dirac wave function for the pseudospin doublets. Besides, these similarities can be maintained well at different deformations.

ACKNOWLEDGMENTS

This work was partly supported by the National Natural Science Foundation of China (No. U2032141), the Open Project of Guangxi Key Laboratory of Nuclear Physics and Nuclear Technology (No. NLK2022-02), the Central Government Guidance Funds for Local Scientific and Technological Development, China (No. Guike ZY22096024), and the Foundation of Fundamental Research for Young Teachers of Zhengzhou University (JC202041041). The theoretical calculation was supported by the nuclear data storage system in Zhengzhou University.

- [1] J. N. Ginocchio, *Phys. Rep.* **414**, 165 (2005).
- [2] H. Liang, J. Meng, and S.-G. Zhou, *Phys. Rep.* **570**, 1 (2015).
- [3] A. Leviatan and J. N. Ginocchio, *Phys. Lett. B* **518**, 214 (2001).
- [4] S. Shen, H. Liang, J. Meng, P. Ring, and S. Zhang, *Phys. Lett. B* **781**, 227 (2018).
- [5] O. Haxel, J. H. D. Jensen, and H. E. Suess, *Phys. Rev.* **75**, 1766 (1949).
- [6] M. G. Mayer, *Phys. Rev.* **75**, 1969 (1949).
- [7] K. Hecht and A. Adler, *Nucl. Phys. A* **137**, 129 (1969).
- [8] A. Arima, M. Harvey, and K. Shimizu, *Phys. Lett. B* **30**, 517 (1969).
- [9] A. Bohr, I. Hamamoto, and B. R. Mottelson, *Phys. Scr.* **26**, 267 (1982).
- [10] J. Dudek, W. Nazarewicz, Z. Szymanski, and G. A. Leander, *Phys. Rev. Lett.* **59**, 1405 (1987).
- [11] W. Nazarewicz, P. J. Twin, P. Fallon, and J. D. Garrett, *Phys. Rev. Lett.* **64**, 1654 (1990).
- [12] T. Byrski, F. A. Beck, D. Curien, C. Schuck, P. Fallon, A. Alderson, I. Ali, M. A. Bentley, A. M. Bruce, P. D. Forsyth, D. Howe, J. W. Roberts, J. F. Sharpey-Schafer, G. Smith, and P. J. Twin, *Phys. Rev. Lett.* **64**, 1650 (1990).
- [13] O. Castaños, M. Moshinsky, and C. Quesne, *Phys. Lett. B* **277**, 238 (1992).
- [14] C. Bahri, J. P. Draayer, and S. A. Moszkowski, *Phys. Rev. Lett.* **68**, 2133 (1992).
- [15] A. L. Blokhin, C. Bahri, and J. P. Draayer, *Phys. Rev. Lett.* **74**, 4149 (1995).
- [16] J. N. Ginocchio, *Phys. Rev. Lett.* **78**, 436 (1997).
- [17] J. N. Ginocchio and D. G. Madland, *Phys. Rev. C* **57**, 1167 (1998).
- [18] J. Meng, K. Sugawara-Tanabe, S. Yamaji, P. Ring, and A. Arima, *Phys. Rev. C* **58**, R628 (1998).
- [19] J. Meng, K. Sugawara-Tanabe, S. Yamaji, and A. Arima, *Phys. Rev. C* **59**, 154 (1999).
- [20] C.-Y. Song, J.-M. Yao, and J. Meng, *Chin. Phys. Lett.* **26**, 122102 (2009).
- [21] C.-Y. Song and J.-M. Yao, *Chin. Phys. Lett.* **34**, 1425 (2010).
- [22] C.-Y. Song, J.-M. Yao, and J. Meng, *Chin. Phys. Lett.* **28**, 092101 (2011).
- [23] T.-T. Sun, W.-L. Lu, and S.-S. Zhang, *Phys. Rev. C* **96**, 044312 (2017).
- [24] W.-L. Lu, Z.-X. Liu, S.-H. Ren, W. Zhang, and T.-T. Sun, *J. Phys. G: Nucl. Phys.* **44**, 125104 (2017).
- [25] S.-G. Zhou, J. Meng, and P. Ring, *Phys. Rev. Lett.* **91**, 262501 (2003).
- [26] I. N. Mishustin, L. M. Satarov, T. J. Bürvenich, H. Stöcker, and W. Greiner, *Phys. Rev. C* **71**, 035201 (2005).
- [27] X. T. He, S. G. Zhou, J. Meng, E. G. Zhao, and W. Scheid, *Eur. Phys. J. A* **28**, 265 (2006).
- [28] H. Liang, W.-H. Long, J. Meng, and N. Van Giai, *Eur. Phys. J. A* **44**, 119 (2010).
- [29] J.-Y. Guo, R.-D. Wang, and X.-Z. Fang, *Phys. Rev. C* **72**, 054319 (2005).
- [30] J. Y. Guo and X. Z. Fang, *Phys. Rev. C* **74**, 024320 (2006).
- [31] S.-S. Zhang, B.-H. Sun, and S.-G. Zhou, *Chin. Phys. Lett.* **24**, 1199 (2007).
- [32] B.-N. Lu, E.-G. Zhao, and S.-G. Zhou, *Phys. Rev. Lett.* **109**, 072501 (2012).
- [33] B.-N. Lu, E.-G. Zhao, and S.-G. Zhou, *Phys. Rev. C* **88**, 024323 (2013).
- [34] Q. Liu, Z.-M. Niu, and J.-Y. Guo, *Phys. Rev. A* **87**, 052122 (2013).
- [35] T.-T. Sun, W.-L. Lu, L. Qian, and Y.-X. Li, *Phys. Rev. C* **99**, 034310 (2019).
- [36] X.-X. Shi, Q. Liu, J.-Y. Guo, and Z.-Z. Ren, *Phys. Lett. B* **801**, 135174 (2020).
- [37] Q. Liu, Y. Zhang, and J.-Y. Guo, *Phys. Lett. B* **824**, 136829 (2022).
- [38] H. Liang, P. Zhao, Y. Zhang, J. Meng, and N. V. Giai, *Phys. Rev. C* **83**, 041301(R) (2011).
- [39] F.-Q. Li, P.-W. Zhao, and H.-Z. Liang, *Chin. Phys. C* **35**, 825 (2011).
- [40] H. Liang, S. Shen, P. Zhao, and J. Meng, *Phys. Rev. C* **87**, 014334 (2013).
- [41] S. Shen, H. Liang, P. Zhao, S. Zhang, and J. Meng, *Phys. Rev. C* **88**, 024311 (2013).
- [42] B. Mottelson, *Nucl. Phys. A* **522**, 1 (1991).
- [43] K. Sugawara-Tanabe and A. Arima, *Phys. Rev. C* **58**, R3065 (1998).
- [44] K. Sugawara-Tanabe, S. Yamaji, and A. Arima, *Phys. Rev. C* **65**, 054313 (2002).
- [45] K. Sugawara-Tanabe, S. Yamaji, and A. Arima, *Phys. Rev. C* **62**, 054307 (2000).
- [46] G. A. Lalazissis, Y. K. Gambhir, J. P. Maharana, C. S. Warke, and P. Ring, *Phys. Rev. C* **58**, R45 (1998).
- [47] J. N. Ginocchio, A. Leviatan, J. Meng, and S.-G. Zhou, *Phys. Rev. C* **69**, 034303 (2004).
- [48] J. Y. Guo, S. W. Chen, Z. M. Niu, D. P. Li, and Q. Liu, *Phys. Rev. Lett.* **112**, 062502 (2014).
- [49] Y. Zhang, Y.-X. Luo, Q. Liu, and J.-Y. Guo, *Phys. Lett. B* **838**, 137716 (2023).
- [50] T. T. Sun, S. Q. Zhang, Y. Zhang, J. N. Hu, and J. Meng, *Phys. Rev. C* **90**, 054321 (2014).
- [51] T.-T. Sun, Z.-M. Niu, and S.-Q. Zhang, *J. Phys. G: Nucl. Phys.* **43**, 045107 (2016).
- [52] S.-H. Ren, T.-T. Sun, and W. Zhang, *Phys. Rev. C* **95**, 054318 (2017).
- [53] X. Y. Qu and Y. Zhang, *Phys. Rev. C* **99**, 014314 (2019).
- [54] X. Y. Qu, H. Tong, and S. Q. Zhang, *Phys. Rev. C* **105**, 014326 (2022).
- [55] H. Oba and M. Matsuo, *Phys. Rev. C* **80**, 024301 (2009).
- [56] Y. Zhang, M. Matsuo, and J. Meng, *Phys. Rev. C* **83**, 054301 (2011).
- [57] T.-T. Sun, *Sci. Sin. Phys. Mech. Astron.* **46**, 012006 (2016).
- [58] T.-T. Sun, Z.-X. Liu, L. Qian, B. Wang, and W. Zhang, *Phys. Rev. C* **99**, 054316 (2019).
- [59] M. Matsuo, *Nucl. Phys. A* **696**, 371 (2001).
- [60] M. Matsuo, K. Mizuyama, and Y. Serizawa, *Phys. Rev. C* **71**, 064326 (2005).
- [61] M. Matsuo and Y. Serizawa, *Phys. Rev. C* **82**, 024318 (2010).
- [62] H. Shimoyama and M. Matsuo, *Phys. Rev. C* **84**, 044317 (2011).
- [63] H. Shimoyama and M. Matsuo, *Phys. Rev. C* **88**, 054308 (2013).
- [64] M. Matsuo, *Phys. Rev. C* **91**, 034604 (2015).
- [65] E.-B. Huo, K.-R. Li, X.-Y. Qu, Y. Zhang, and T.-T. Sun, *Nucl. Sci. Tech.* **34**, 105 (2023).
- [66] T.-T. Sun, L. Qian, C. Chen, P. Ring, and Z. P. Li, *Phys. Rev. C* **101**, 014321 (2020).
- [67] C. Chen, Z. P. Li, Y. X. Li, and T.-T. Sun, *Chin. Phys. C* **44**, 084105 (2020).

- [68] Y.-T. Wang and T.-T. Sun, *Nucl. Sci. Tech.* **32**, 46 (2021).
- [69] T.-T. Sun, Z. P. Li, and P. Ring, *Phys. Lett. B* **847**, 138320 (2023).
- [70] T.-T. Sun, and Z. P. Li, [arXiv:2311.14765](https://arxiv.org/abs/2311.14765).
- [71] I. Hamamoto, *Phys. Rev. C* **69**, 041306(R) (2004).
- [72] Z. P. Li, J. Meng, Y. Zhang, S. G. Zhou, and L. N. Savushkin, *Phys. Rev. C* **81**, 034311 (2010).
- [73] B. Pritychenko, M. Birch, B. Singh, and M. Horoi, *At. Data Nucl. Data Tables* **107**, 1 (2016).